

Synthesis of TiO₂/ZnO photoanodes on FTO conductive glass for photovoltaic applications

V. F. Nunes^{1*}, F. M. Lima¹, E. S. Teixeira¹, P. H. F. Maia Júnior¹, A. F. L. Almeida², F. N. A. Freire¹

¹Federal University of Ceará, Department of Science and Engineering Materials, 60440554, Fortaleza, CE, Brazil

²Federal University of Ceará, Department of Mechanical Engineering, 60455760, Fortaleza, CE, Brazil

Abstract

For oxide semiconductors for application in dye-sensitized solar cells (DSSCs), titanium dioxide conjugated with zinc oxide thin films was synthesized and characterized. The UV (ultraviolet) spectrum characterization showed a peak of absorbance at around 355 nm, with a band gap of 3.25 eV and reflectance around 85%. Such characteristics allowed the fabrication of DSSCs with N719 dye, under simulated light of 100 mW/cm². The highest efficiency of 1.17% was at 5% titanium dioxide and 4 h of dye immersion.

Keywords: ZnO, DSSC, titanium oxide, dye time.

INTRODUCTION

Photovoltaic (PV) energy is a viable option for renewable energy, supplying demands for houses, cars, and industries. Countries such as India intend to make commercial cars green by 2030 [1]. Dye-sensitized solar cells (DSSCs) are part of the third generation of photovoltaic solar cells. The DSSC constitutes a photoanode, a counter electrode, a dye, and an electrolyte [2]. The photon excited in the dye circulates through the photoanode, the external circuit, and back to the electrolyte. The photoanode is on a transparent conductor oxide, such as fluorine tin oxide (FTO), graphite, or platinum. Zinc oxide has many advantages for the photoelectric effect, such as low-cost, non-toxicity, high visibility, light transmittance, and low resistivity after doping [3]. Oxides are optional to the Si-based photovoltaic technologies that are already established. However, the lower electron injection into the ZnO can reduce the photocurrent efficiency (PCE) [4]. Anand et al. [5] produced 1.652 mA with DSSC based on the ZnO nanoflower shape. The energy conversion was at 1.61% with ZnO/ruthenium-based dye [6]. These results can be improved when combining ZnO with other oxide semiconductors. Many works have mixed ZnO with oxides containing elements such as tin (Sn), titanium (Ti), aluminum (Al), cobalt (Co), and gallium (Ga), amongst others [7-18]. TiO₂ is a viable option with ZnO due to similarities between the two oxides, like the band gap energy value, around 3.0 eV for TiO₂ and 3.2 eV for ZnO [19]. The blend between ZnO and TiO₂ has high electron injection, besides the high electron-hole separation in the TiO₂ [20]. The adsorption dye time of the films can also affect the performance of the solar cells. The dye adsorption may enhance the electron density and electron transfer in


the film and the electrolyte interface [21]. The time for dye immersion should be enough to cover the layer of the film and avoid the deterioration of the cell, due to the formation of Zn²⁺/dye aggregates that lower electron injection [22, 23].

In this work, TiO₂-ZnO thin films were synthesized on FTO to improve the photocurrent activity and the effect of dye adsorption time on the film's efficiency. The main novelty of this work is the simple, low-cost, environmentally friendly, and simple synthesis of crystallite thin films. Methods that deposit zinc oxides and titanium oxides are spray pyrolysis, spin coating, hydrothermal deposition, and doctor blade. The present methodology uses none of the usual additional chemical reactants or/and supportive elements, like heat and vacuum, nor expensive deposition devices, which reduces the total cost of the solar cell. Since cost and efficiency are crucial for the photovoltaic industry advancement, this methodology can enhance the DSSC's technology, lowering the overall production costs. Titanium dioxide/zinc oxide thin films were synthesized by simply dipping the glass into the precursor solution and waiting until complete evaporation of the solvent, without any additives, at room temperature, and with no auxiliary or additional devices. The characterization of the DSSCs indicated the performance of the assembled cells.

EXPERIMENTAL

Synthesis of the TiO₂/ZnO films: all reagents were used without further purification: TiO₂ (rutile, Sigma-Aldrich) and ZnO (Vetec). 0.05 g of ZnO powder was dispersed in 10 mL of deionized water and then placed in an ultrasonic bath for 30 min. Three different suspensions of ZnO with 5, 10, and 15 wt% of rutile (TiO₂) were prepared, which were then used to cover a fluorine-doped tin oxide (FTO) glass (Solaronix) until complete evaporation of the water. The layers of the oxides that remained on the FTO were then submitted to thermal treatment at 450 °C for 30 min.

* vanjafnunes@gmail.com

 <https://orcid.org/0000-0003-2458-5616>

Characterization of the films: the films of ZnO/TiO₂ were characterized by X-ray diffraction (DMAXB, Rigaku) with CuK α radiation between 20° and 70° (2 θ). The UV-vis analysis of the films was performed between 220 and 700 nm by spectroscopy (UV-2600, with integrating sphere ISR-2600Plus, Shimadzu). Also, scanning electron microscopy (SEM) was performed (Quanta FEG 450, FEI) at 50000 times magnification and 20 kV.

DSSC fabrication: the films of titanium dioxide/zinc oxide were deposited on FTO, as the electrode, and the counter electrode was platinum (Solaronix) deposited also on FTO. The films, before being connected with the counter electrode, were immersed in N719 dye (Solaronix) at a concentration of 3x10⁻⁴ M. The films were immersed in the dye for 4 and 24 h, for the three concentrations, and then sandwiched and coupled with the counter electrode. The electrolyte used between them was Iodolyte AN-50 (Solaronix). The assembled cells were electrically characterized on a potentiostat (Autolab PGSTAT302N, Metrohm) under 100 mW/cm² illumination, for measurement of the I-V curves.

RESULTS AND DISCUSSION

SEM analysis: Figs. 1 and 2 show the images obtained by scanning electron microscopy (SEM) of the nanocrystallite blend of titanium oxide and zinc oxide. The combination created the nanocrystallite films with the thickness listed in Table I, which was calculated using the SEM images (Fig. 1) and the following equations [24, 25]:

$$\alpha \approx F_{(K-M)}(R) = \frac{(1-R)^2}{2R} \quad (A)$$

$$\alpha = \frac{1}{d} \cdot \ln \frac{(1-R)^2}{T} \quad (B)$$

There was no substantial difference between the SEM images, with the formation of agglomerates for all percentages of Ti(IV), probably due to the high adhesion forces between the particles [26]. The values for thickness varied between 6 and 20 μ m; Homcheunjit et al. [24] also observed differences in thickness from 8 to 20 μ m, when depositing thin films by spray pyrolysis and dip coating. These results showed the importance of finding an optimum thickness. When it is too thick, the film at 15%, there are conglomerates that block the electron passage through the film and may increase the resistance to the photocurrent flow. Otherwise, if the film is too thin, the film does not absorb the dye, causing a lower flux of photon-excited electrons in the photoanode through the external circuit. The concentration of titanium affects the building of the crystallite layers, which can affect the porosity of the nanocrystallites, and, as noted by Zhou et al. [27], there must be an equilibrium between porosity and cell efficiency. The higher TiO₂ concentration presented less evident porous (Fig. 1a), which may have

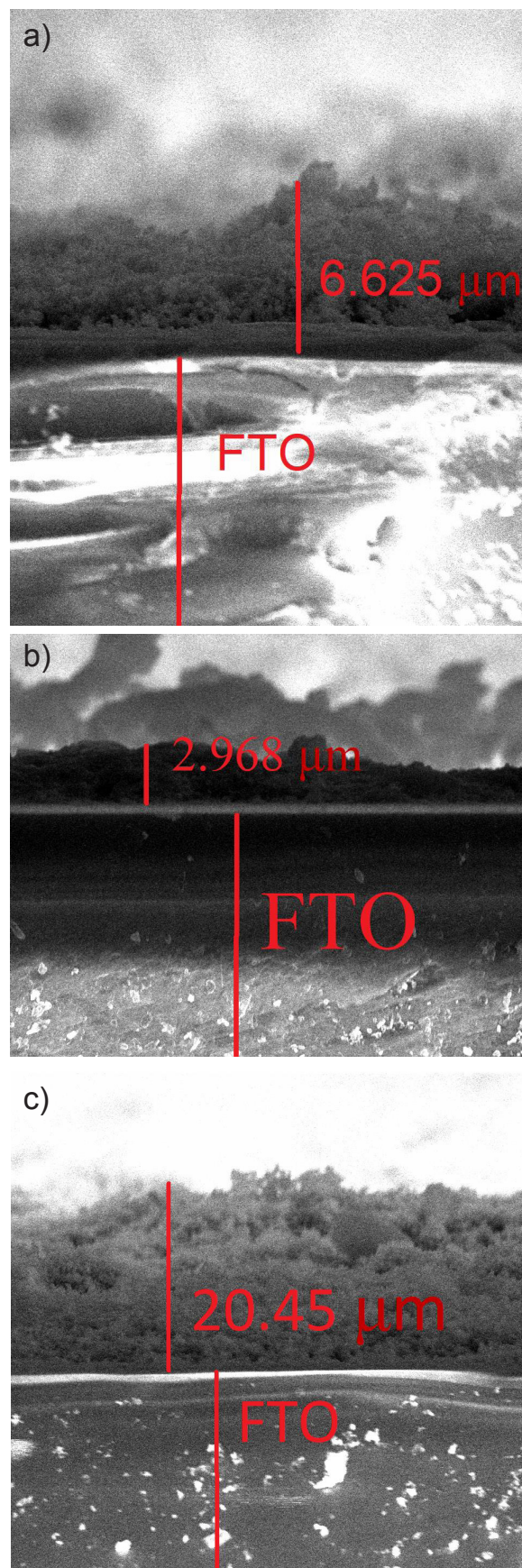


Figure 1: SEM images of the cross-section of the films with: a) 5% Ti(IV); b) 10% Ti(IV); and c) 15% Ti(IV).

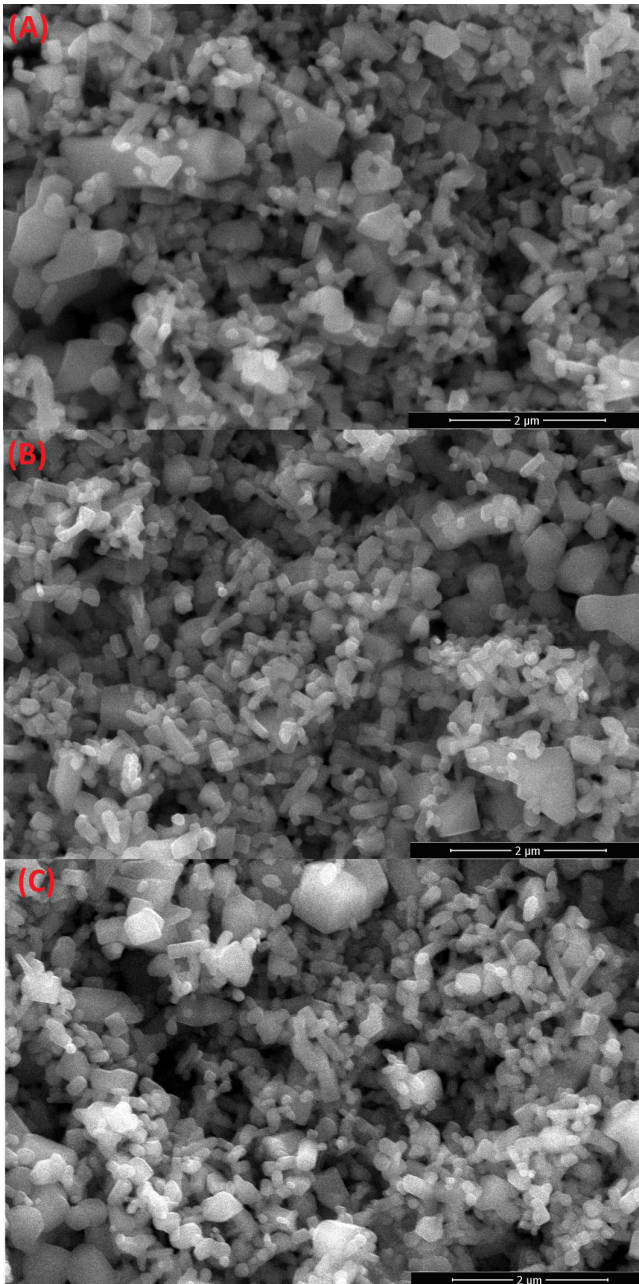


Figure 2: SEM micrographs for the thin films with: a) 5% TiO₂; b) 10% TiO₂; and c) 15% TiO₂.

Table I - Thickness of the TiO₂/ZnO thin films.

Thin film (%TiO ₂)	5%	10%	15%
Thickness (μm)	6.62	2.97	20.45

negatively influenced the short current density of the cell at 15% concentration [27].

X-ray diffraction (XRD): the XRD patterns showed the wurtzite structure for the zinc oxide, corresponding to the ICSD file 67848 (Fig. 3). The characteristic peaks corresponded to the crystalline planes (100), at around 31.7°, (002), 34°, (101), 36.2°, (102), 47.5°, (110), 56.5°, (103), 62.7°, and (112), 67.8°. The more prominent peak was the

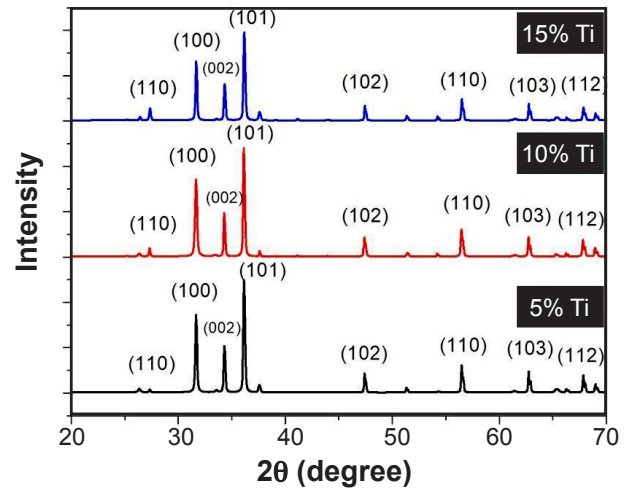


Figure 3: XRD patterns of the synthesized films, at the three different percentages.

(101), 36.2°, as also observed by Bhushan et al. [28]. At a higher percentage of titanium dioxide, the intensity of the (002) peak decreased. The three characteristic peaks, (100), (002), and (101), all had narrow widths, which attested to the crystallinity of the synthesized films [29]. The (110) peak at around 26° identified the rutile phase of the TiO₂ [30].

From the XRD data, the Scherrer equation ($D = k\lambda/\beta\cos\theta$) was used to calculate the crystallite size (D), where k is 0.9, λ is the wavelength (1.5406 Å), β is the broadening of the diffraction line at the half intensity, and θ is the Bragg's diffraction angle [31]. According to this data, by increasing the mass percentage of titanium dioxide, the average crystallite size also increased, from 53.1 nm at 5% to 54.8 nm at 10% and 55.8 nm at 15% Ti(IV). Aksoy et al. [23] obtained crystallite sizes of 34 nm for the powder and 46 nm for the thin film, both of pure ZnO, indicating that the annealing treatment of 400 °C was responsible for the increase in the average size. The authors calculated the grain sizes of titanium dioxide heated between 100 to 600 °C, for the anatase and rutile phases, with results between 49.27 to 61.91 nm [32]. The present results, at 450 °C, were close to the results between 400 and 500 °C. For larger grain sizes, there is an increase in the crystallinity of the structures [31]. Other techniques like spray pyrolysis, co-precipitation, DC magnetron sputtering, sol-gel, spin coating, and thermal synthesis obtained sizes of 34.7, 32, 23.66, 42-47, and 14 nm [1, 18, 33-35]. The large crystallite sizes in this work can be explained by the high concentration of titanium dioxide, above 10%, and the heat treatment at 450 °C [17]. Table II lists the specific surface area (SSA) [20]. The values for the crystallite sizes (D) and the ZnO density (ρ) were used for the calculation (Eq. C). The SSA indicates the amount of TiO₂ in the ZnO matrix. Higher SSA points to improved electron transport and photovoltaic efficiency, as was noticed by the better efficient cell at 5% TiO₂, with an SSA of 20.1 m²/g. The lower value of the SSA can also explain the lower incorporation of the Ti⁴⁺ and, consequently, higher thickness.

$$SSA = \frac{6000}{\rho \cdot D} \quad (C)$$

Table II - SSA and dimension for the nanostructures.

TiO ₂ (%)	5	10	15
Crystallite size (nm)	53.1	54.8	55.8
SSA (m ² /g)	20.1	19.5	19.2

UV-vis studies: the absorbance plot demonstrated peaks at the UV region for the films (Fig. 4a). The peaks were at around 250 nm with 5% titanium. For the 10% and 15% titanium-doped films, there was also a peak at about 355 nm, associated with the presence of Ti⁴⁺ [36]. There was a peak at around the same wavelength value (~350 nm) for the isolated alcohol N719 dye solution (Fig. 4b) that indicated that the oxide conduction band was close to the dye conduction band, making possible the electron transition inside the cell. Also, for the 5% Ti, the film had higher absorption in the UV region. Upadhyay *et al.* [37] also reported a sharp band on the spectrum at less than 400 nm. The smaller crystallite

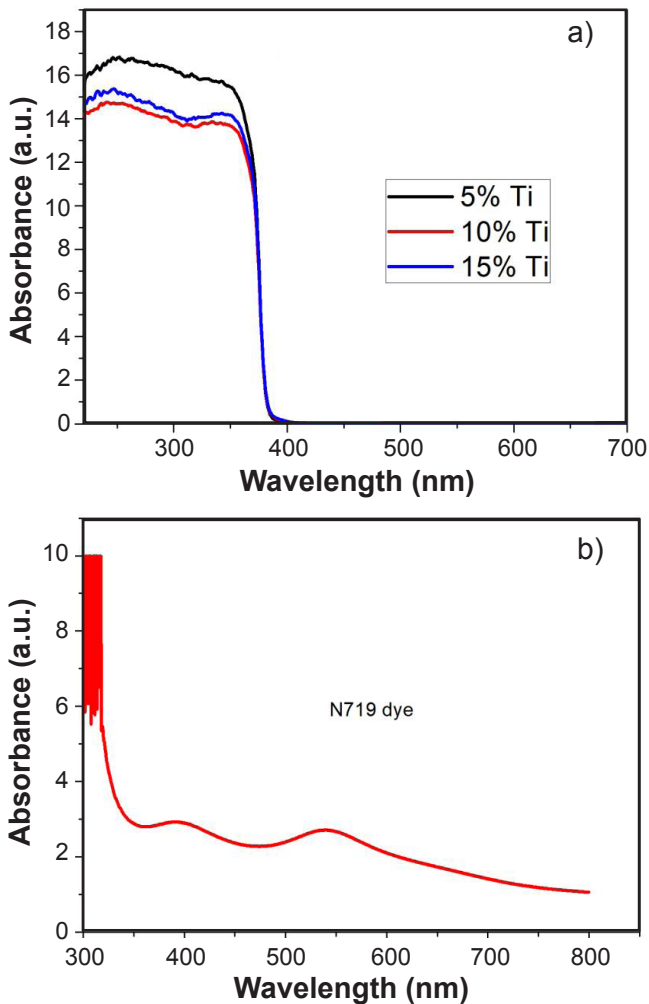


Figure 4: Absorbance spectra of: a) nanostructures; and b) isolated dye solution.

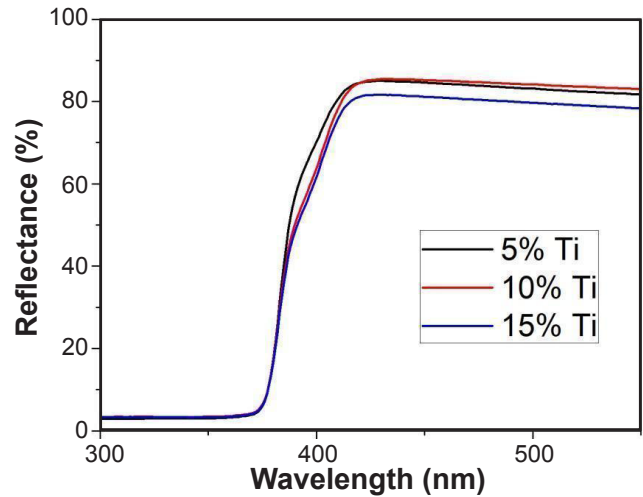


Figure 5: Reflectance spectra of the photoanodes.

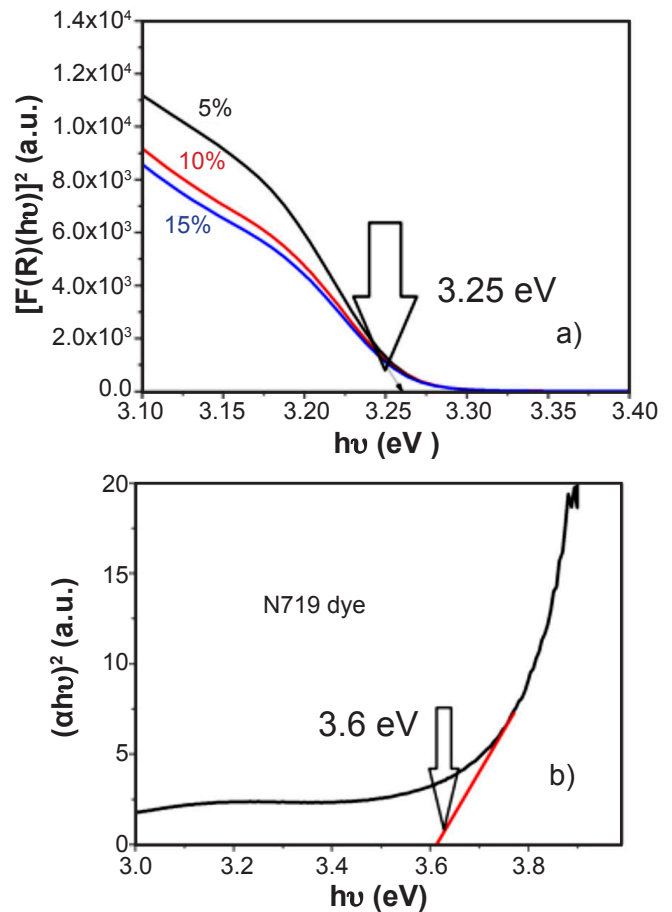


Figure 6: Tauc plots of the Kubelka-Munk function for: a) semiconductor layers; and b) N719 dye.

size agreed with the maximum absorbance at 5% TiO₂ [1]. The reflectance for all samples was around the same value, about 83% (Fig. 5). The Ti(IV) percentages did not alter the reflectance of the ZnO, with a slight decrease for the ZnO at 15% TiO₂. Das *et al.* [21] observed similar values of reflectance for Al/ZnO treated at 800 °C. The Kubelka-Munk function $F(R)$ was used to calculate the band gap for

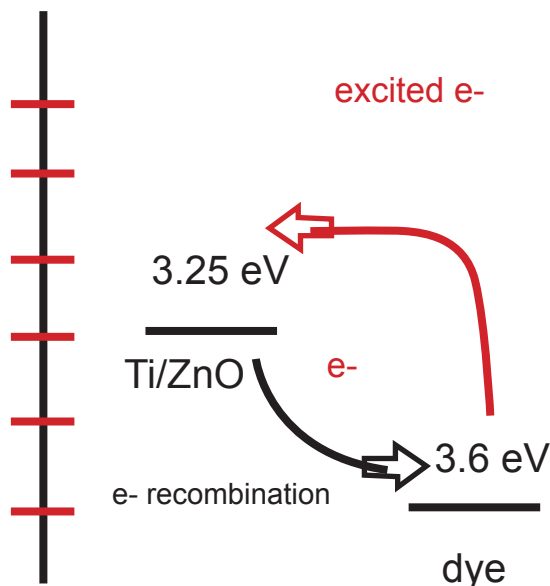


Figure 7: Schema of electron transition and recombination inside the cell.

the films [38]. A plot of $[F(R)(h\nu)]^2$ as a function of photon energy, $h\nu$, made possible the determination of the band gap energy (E_g) from the curve extrapolation to the x-axis. The band gap was around 3.25 eV for the three films (Fig. 6). Ali et al. [36] found 3.255 eV for Ti-doped ZnO by the sputter deposition technique [39]. Also, it was found 3.17 and 3.30 eV for ZnO-TiO₂ composites prepared by sol-gel at 15% and 25% TiO₂. The layers of ZnO/TiO₂ and N719 dye had levels of band gap between 3.25 and 3.6 eV, respectively (Fig. 7). It can help the electron transition. At the same time, it can increase the recombination rate which reduces cell efficiency.

The photoluminescence (PL) spectra in Fig. 8 show a quenching peak for the films at about 385 nm, with the peak for the 5% film shifted closer to the visible, which helps improve efficiency. Katta et al. [40] observed a PL peak at 405 nm for a non-doped TiO₂. The blend of the titanium oxide helped to shift the ZnO PL spectrum. Fig. 9 indicates the Urbach energy between 1.5 and 1.6 eV for the three TiO₂/ZnO blends. The increase in the Urbach energy from 5% to 15% TiO₂ revealed an increase in the formation of oxygen vacancies and the number of sites of trapping states

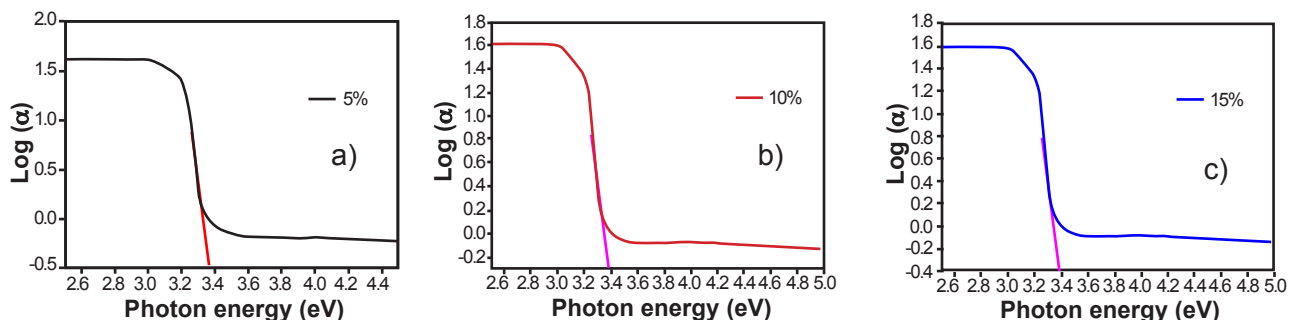


Figure 9: Graphs of absorption coefficient (α) versus photon energy ($h\nu$) for the determination of Urbach energy for the blend TiO₂/ZnO nanofilms.

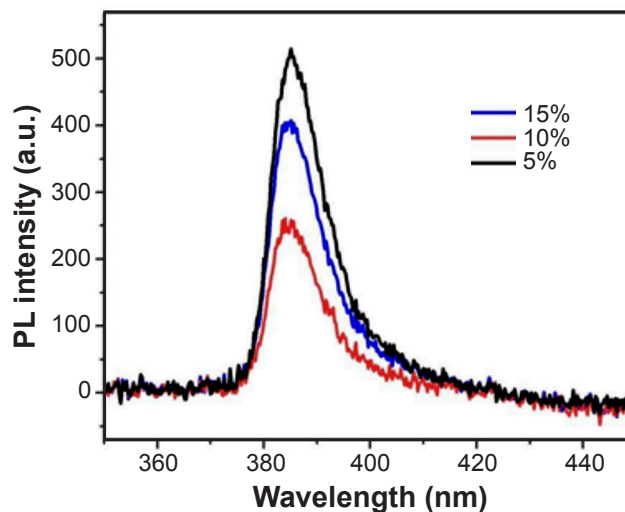


Figure 8: PL fluorescence spectra of TiO₂/ZnO films.

which can form dye aggregations and increase the resistance to the electron flux [40].

Nyquist plot: Fig. 10 shows the Nyquist plot for the thin films at different dye loading times, 4 and 24 h. The imaginary part plotted against the real part exhibited semicircular shapes for the 24 h plot (Fig. 10b), but for 4 h (Fig. 10a), the plot did not close the arc. In both cases, the values indicated high resistance in the interfaces.

Photovoltaic tests: the efficiency observed by Das et al. [21] for a sample obtained by co-precipitation and CuO was around 0.89%. The incorporation of TiO₂ improved the short-circuit current density (J_{sc}) and the overall efficiency (η). The presence of the titanium improved the light-harvesting efficiency, with lower charge rate recombination, and increased the transfer of electrons from the ZnO to the FTO, improving the J_{sc} and the open-circuit voltage (V_{oc}) [41]. From the data collected, the optimum value of Ti(IV) in these synthesis conditions was at 5 wt%, with an efficiency of 1.17% and J_{sc} of 4.58 mA/cm² (Fig. 11). The efficiency was close to the ones found by Pham et al. [42], where a conversion of 0.7% was reached for SnO₂@TiO₂ shells applied to DSSCs with an aqueous electrolyte. Ako et al. [43] created TiO₂/ZnO core-shell nanostructures photoanodes with a η value of 0.53%. The increase in the fill factor (FF) to 0.56 (at 10 wt% TiO₂) suggested lower recombination between the photoanode and the I₃⁻/I₃⁻ [15].

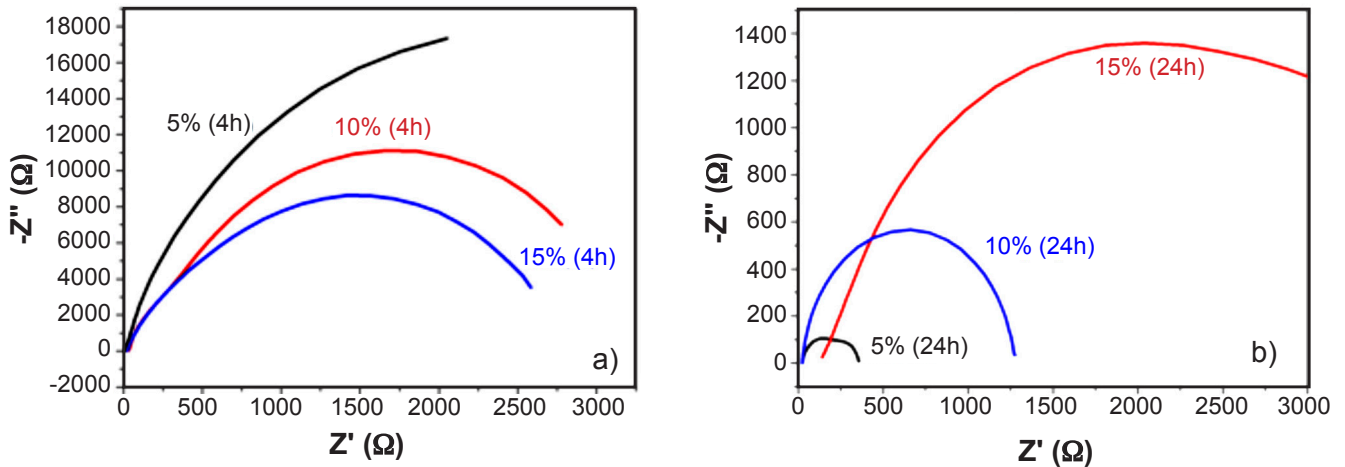
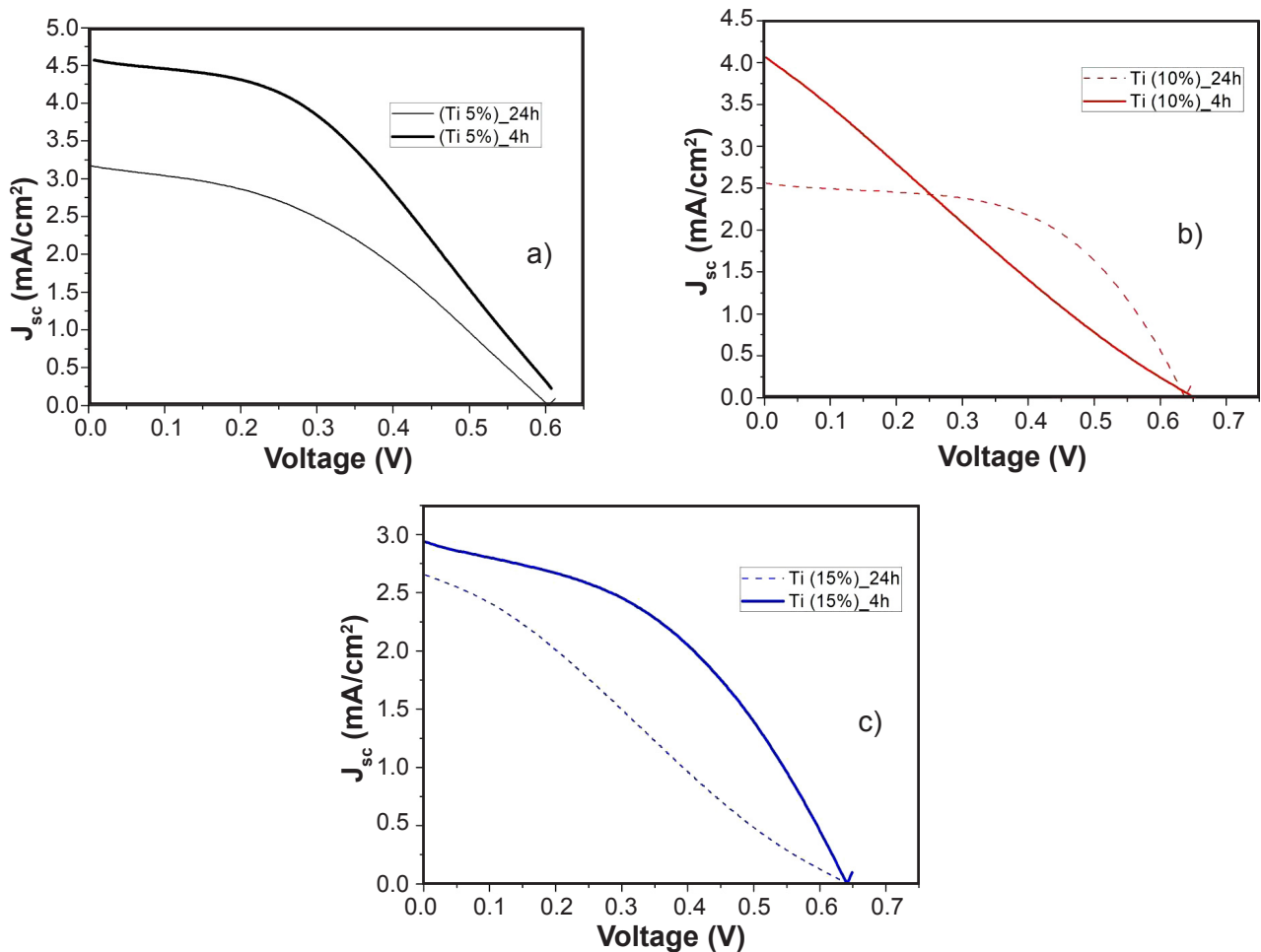


Figure 10: Nyquist plots of thin films for 4 h (a) and 24 h (b) dye immersion time

Figure 11: Short-circuit current density (J_{sc}) versus voltage for 5 wt% (a), 10 wt% (b), and 15 wt% (c) TiO₂/ZnO.

Efficiency and fill factor were according to Tyagi *et al.* [41]. Table III relates the photovoltaic parameters found for the cells with photoanodes on the dye for 4 and 24 h. The shorter time on dye was beneficial for the increase in short-circuit current density for all the percentages of TiO₂, increasing the efficiency, except for the 10% TiO₂ film. The decrease in efficiency was due to the lowering of FF, from 0.56 to 0.23, indicating that the average voltage and J_{sc} of this cell did not

follow the maximum current and voltage, with a steep along the way, decreasing in values (Fig. 11b). At 15 wt% TiO₂, the efficiency value almost doubled, led by the higher J_{sc} and a higher fill factor, from 0.28 to 0.43 (Fig. 11c). The benefits of the lower dye immersion time were usual for large crystallite sizes. When the crystallite is large, more dye time can create aggregates that hinder the flow of excited electrons through the cell. The formation of agglomerates can increase the

Table III - Photovoltaic parameters for TiO₂/ZnO films.

Sample	V _{oc} (V)	FF	J _{sc} (mA/cm ²)	η (%)
Ti 5% 24 h	0.61	0.40	3.17	0.77
Ti 5% 4 h	0.63	0.40	4.58	1.17
Ti 10% 24 h	0.64	0.56	2.56	0.88
Ti 10% 4 h	0.65	0.23	4.05	0.63
Ti 15% 24 h	0.64	0.28	2.65	0.45
Ti 15% 4 h	0.65	0.43	3.00	0.84

V_{oc}: open-circuit voltage; FF: fill factor; J_{sc}: short-circuit current density; η: cell efficiency.

resistance to electron mobility, lowering the J_{sc} values [44].

Table IV compares the best efficiency for this work and photovoltaic efficiencies obtained by other authors, using TiO₂ and other elements, showing the methodology for the film's synthesis works for the photovoltaic application. Tyagi *et al.* [41] found photovoltaic parameters for non-doped ZnO-based DSSCs from 0.16% to 0.64% efficiency and a current density of 1.62 mA/cm². Mehmood *et al.* [45] obtained higher efficiency for the ZnO-based DSSCs doped with titanium (1%) and Cu, reaching 2.38% efficiency. Katta *et al.* [40] also concluded that for the doped TiO₂, the photocurrent density was three times higher than the non-doped photoanode. Yang *et al.* [46] obtained an efficiency of 3.61% for 1D ZnO@C@MoS₂ nanoarrays on conductive glass. Yu and Zi [47] decorated ZnO hollow microspheres with TiO₂ nanotubes with an efficiency of 7.40%. Thus, these works reaffirm that the semiconductor oxides can improve their characteristics when incorporated with n-type materials. The recombination between the TiO₂/electrolyte caused low efficiency, as indicated by the semicircles in Fig. 10 [48]. This recombination happened due to the back recombination of charges between the dye and the counter electrode FTO [49]. Also, in accordance with Ekmekci *et al.* [50], the overall efficiency of the DSSC was better for a lower concentration of titanium. Table IV indicates that this work methodology reached the levels of efficiency obtained by more sophisticated, complex, and expensive deposition methods. The present work was on par with the current efficiency in the research community.

Table IV - Efficiency values for different DSSCs.

Efficiency (%)	Ref.
1.17	This work
0.70	[27]
0.89	[15]
0.53	[28]
2.38	[44]
7.56	[17]

CONCLUSIONS

TiO₂/ZnO thin films were synthesized by simply dipping the FTO into the precursor suspensions and waiting until

complete evaporation of the liquid (water), without any additives at room temperature and with no auxiliary or additional devices. This method proved, by analysis such as X-ray diffraction, SEM, absorbance, and band gap, the formation of nanocrystalline-type wurtzite ZnO. The films presented good transmittance and reflectance on the UV-vis spectrum. However, the combination of these films with the N719 dye had poor photovoltaic performance, higher being 1.17%. Future works could improve this value by changing the dye, used in the photovoltaic cell, or the concentration of the TiO₂/ZnO combination.

ACKNOWLEDGMENTS

The authors would like to acknowledge the Brazilian research agency Coordenação de Aperfeiçoamento de Pessoal de Nível Superior-CAPES for the financial support, the Laboratório de Filmes Finos e Energias Renováveis-LAFFER for the assistance throughout the research. Also, the authors want to thank the CNPq (Process: 402561/2007-4) Edital MCT/CNPq n° 10/2007. The authors would like to thank the Central Analítica-UFC (funded by Finep-CT-INFRA, CAPES-Pró-Equipamentos, and MCTI-CNPq-SisNano2.0) for microscopy measurements.

REFERENCES

- [1] M. Bhogaita, D. Devaprakasam, *Solar Energy* **214** (2021) 517.
- [2] H. Widiyandari, S. Wijyanti, A. Prasetio, A. Purwanto, *Opt. Mater.* **107** (2020) 110077.
- [3] F. Yang, J. Song, X. Chen, X. Lu, J. Li, Q. Xue, B. Han, X. Meng, J. Li, Y. Wang, *Solar Energy* **228** (2021) 168.
- [4] K. Kighuta, A.-Y. Gopalan, D.E. Lee, G. Saianand, Y.-L. Hou, S.S. Park, K.P. Lee, J.C. Lee, W.J. Kim, *J. Environ. Chem. Eng.* **9** (2021) 106417.
- [5] A. Anand, S. Mittal, V. Leeladevi, D. De, *Mater. Today Proc.* **27**, 1 (2022) 227.
- [6] M. Biçer, M. Gökçen, E. Orhan, *Opt. Mater.* **131** (2022) 112691.
- [7] M. Abdelfatah, H.Y. Salah, M.I. El-Henawey, A.H. Oraby, A. El-Shaer, W. Ismail, *J. Alloys Compd.* **873** (2021) 159875.
- [8] V. Ganesh, I.S. Yahia, S. Alfaify, M. Shkir, *J. Phys. Chem. Solids* **100** (2017) 115.
- [9] B.B. Çirak, Ç. Eden, Ç. Erdoğan, Z. Demir, K.V. Özdokur, B. Caglar, S.M. Karadeniz, T. Kilingç, A.E. Ekinici, Ç. Çirak, *Optik* **203** (2020) 163963.
- [10] A. Yildiz, T. Serin, E. Öztürk, N. Serin, *Thin Solid Films* **522** (2012) 90.
- [11] M. Ajili, M. Castagné, N.K. Turki, *Superlattices Microstruct.* **53** (2013) 213.
- [12] H. Aydin, H.M. El-Nasser, C. Aydin, A.A. Al-Ghamdi, F. Yakuphanoglu, *Appl. Surf. Sci.* **350** (2015) 109.
- [13] L. Xu, G. Zheng, F. Xian, J. Su, *Mater. Chem. Phys.* **229** (2019) 215.
- [14] M.I. Khan, M. Naeem, G.M. Mustafa, S.A. Abubshait,

- A. Mahmood, W. Al-Masry, N.Y.A. Al-Gharadi, S.M. Ramay, *Ceram. Int.* **46** (2020) 26590.
- [15] Y. Caglar, S. Aksoy, S. Ilican, M. Caglar, *Superlattices Microstruct.* **46** (2009) 469.
- [16] V.F. Nunes, E.S. Teixeira, P.H.F. Maia Júnior, A.F.L. Almeida, F.N.A. Freire, *Cerâmica* **68**, 385 (2022) 120.
- [17] V.F. Nunes, F.M. Lima, E.S. Teixeira, P.H.F.M. Júnior, A.F.L. Almeida, F.N.A. Freire, *Matéria* **26**, 4 (2021) e13112.
- [18] A. Badawi, M.G. Althobaiti, E.E. Ali, S.S. Alharthi, A.N. Alharbi, *Opt. Mater.* **124** (2022) 112055.
- [19] R. Gosh, R.P. Sahu, R. Ganguly, I. Zhitomirsky, I.K. Puri, *Ceram. Int.* **46** (2020) 3777.
- [20] T.D. Malevu, *Phys. B* **621** (2021) 413291.
- [21] A. Das, R.R. Wary, R.G. Nair, *Solid State Sci.* **104** (2020) 106290.
- [22] W.-C. Chang, C.-H. Lee, W.-C. Yu, C.-M. Lin, *Nanoscale Res. Lett.* **7** (2012) 688.
- [23] S. Aksoy, K. Gorgum, Y. Caglar, M. Caglar, *J. Mol. Struct.* **1189** (2019) 181.
- [24] R. Homcheunjit, P. Pluengphon, A. Tubtimtae, P. Teesetsopon, *Phys. B* **637** (2022) 413885.
- [25] M. Patel, A. Chavda, I. Mukhopadhyay, J. Kim, A. Ray, *Nanoscale* **8** (2016) 2293.
- [26] A. Hidayat, A. Taufiq, Z.A.I. Supardi, S.M. Jayadininggar, U. Sa'adah, N.A. Astarini, T. Suprayogi, M. Diantoro, *Mater. Today Proc.* **44** (2021) 3395.
- [27] K. Zhou, M. Spencer, K. Nulph, P. Appiah-Kubi, K.A.S. Fernando, *Solar Energy* **241** (2022) 343.
- [28] M. Bhushan, R. Jha, R. Bhardwaj, R. Sharma, *Mater. Today Proc.* **48** (2022) 629.
- [29] A.H. Javed, N. Shahzad, M.A. Khan, M. Ayub, N. Iqbal, M. Hassan, N. Hussain, M.I. Rameel, M.I. Shahzad, *Solar Energy* **230** (2021) 492.
- [30] R. Sekar, R. Sivasamy, B. Ricardo, P. Manidurai, *Mater. Sci. Semicond. Process.* **132** (2021) 105917.
- [31] M. Thirumoorthi, J.T.J. Prakash, *Mater. Sci. Eng. B* **248** (2019) 11440.
- [32] F.M. Lima, F.M. Martins, P.H.F. Maia Júnior, A.F.L. Almeida, F.N.A. Freire, *Rev. Matér.* **23** (2017) e11965.
- [33] E. Kouhestanian, S.A. Mozaffari, M. Ranjbar, H.S. Amoli, *Org. Electron.* **86** (2020) 105915.
- [34] T. Marimuthu, N. Anandhan, R. Thangamuthu, S. Surya, *J. Alloys Compd.* **693** (2017) 1011.
- [35] D.S. Biron, V. dos Santos, C.P. Bergmann, *Mater. Res.* **23** (2020) e20200080.
- [36] M.M. Ali, M.J. Haque, M.H. Kabir, M.A. Kaiyum, M.S. Rahman, *Results Mater.* **11** (2021) 100199.
- [37] G.K. Upadhyay, J.K. Rajput, T.K. Pathak, V. Kumar, L.P. Purohit, *Vacuum* **160** (2019) 154.
- [38] S. Aksoy, O. Polat, K. Gorgun, Y. Caglar, M. Caglar, *Phys. E* **121** (2020) 114127.
- [39] C. Bairam, Y. Yalçın, H.I. Efkere, E. Çokduygular, Ç. Çetinkaya, B. Kinaci, S. Özçelik, *Phys. B* **616** (2021) 413126.
- [40] V.S. Katta, A. Das, R.D. K. G. Cilaveni, S. Pulipaka, G. Veerappan, E. Ramasamy, P. Meduri, S. Ashtana, D. Melepurath, S. Santosh, K. Raavi, *Sol. Energy Mater. Sol. Cells* **220** (2021) 110843.
- [41] J. Tyagi, H. Gupta, L.P. Purohit, *Opt. Mater.* **115** (2021) 111014.
- [42] B. Pham, D. Willinger, N.K. McMillan, J. Roye, W. Burnett, A. D'Achille, J.L. Coffey, B.D. Sherman, *Sol. Energy* **224** (2021) 984.
- [43] R.T. Ako, D.S.U. Peiris, P. Ekanayake, A.L. Tan, D.J. Young, Z. Zheng, V. Chellappan, *Sol. Energy Mater. Sol. Cells* **157** (2016) 18.
- [44] H.A. Deepa, G.M. Madhu, V. Venkatesham, *Mater. Today Proc.* **46** (2021) 4579.
- [45] B. Mehmood, M.I. Khan, M. Iqbal, A. Mahmood, W. Al-Masry, *Int. J. Energy Res.* **45** (2021) 2445.
- [46] F. Yang, Y. Gao, P. Zhao, Y. He, Y. Wang, *Mater. Lett.* **324** (2022) 132716.
- [47] L. Yu, Z. Zi, *Mater. Sci. Semicond. Process.* **149** (2022) 106881.
- [48] S. Erten-Ela, Y. Ueno, T. Asaba, Y. Kubo, *New J. Chem.* **41** (2017) 10367.
- [49] S. Erten-Ela, A.C. Cakir, *Energy Sources A* **37** (2015) 807.
- [50] M. Ekmekci, C. Ela, S. Erthen-Ela, *Appl. Ceram. Technol.* **16** (2019) 727.
- (*Rec.* 21/07/2022, *Rev.* 27/10/2022, 16/01/2023, *Ac.* 21/01/2023)